AIAA SPACE Forum
13 - 16 September 2016, Long Beach, California
AIAA SPACE 2016

10.2514/6.2016-5498

HF Vector Sensor for Radio Astronomy: Ground Testing Results

Mary Knapp[1]
Massachusetts Institute of Technology, Department of Earth, Atmospheric, and Planetary Science, Cambridge, MA 02139

Ryan Volz[2] and Frank D. Lind[3]
MIT Haystack Observatory, Westford, MA

and

Frank C. Robey[4], Alan J. Fenn[5], Kerry Johnson[6], Mark Silver[7], Alex Morris[8], and Sarah Klein[9]
Lincoln Laboratory, Lexington, MA

The radio sky below ~10 MHz is largely unexplored due to the inability of ground-based telescopes to observe near or below the ionospheric plasma frequency, or cut-off frequency. A space-based interferometric array is required to probe the portion of the electromagnetic (E-M) spectrum below 10 MHz with sufficient angular resolution and sensitivity to be scientifically useful. Multi-spacecraft constellations scale quickly in cost and complexity as the number of spacecraft increases, so minimizing the number of required spacecraft for an interferometric array (while maintaining performance) is critical for feasibility. We present the HF (High Frequency, 3 to 30 MHz) Vector Sensor as a high performance spacecraft instrument in a future space-based interferometric array. The HF Vector Sensor is composed of three orthogonal dipoles and three orthogonal loop antennas with a common phase center. These six elements fully measure the E-M field of incoming radiation. We present the design of two prototype HF Vector Sensors, ground-based data collection at frequencies above the ionospheric cut-off, and imaging results using several different algorithms.

Nomenclature

HF = high frequency (3 to 30 MHz)
MF = medium frequency (300 kHz to 3 MHz)
VS = vector sensor

[1] PhD Candidate, Department of Earth, Atmospheric, and Planetary Science, MIT, 77 Massachusetts Avenue Cambridge, MA 02139.
[2] Postdoctoral Associate, MIT Haystack Observatory, 99 Millstone Rd, Westford, MA, 01886, N/A.
[3] Research Engineer, MIT Haystack Observatory, 99 Millstone Road, Westford MA 01886 USA.
[4] Associate Group Leader, MIT Lincoln Laboratory, 244 Wood St., Lexington, MA 02420 .
[5] Senior Staff, MIT Lincoln Laboratory, Massachusetts Institute of Technology, 244 Wood Street, Lexington, MA, USA.
[6] Associate staff, MIT Lincoln Laboratory, 244 Wood St. Lexington, MA 02420
[7] Technical Staff, Mechanical Engineering, MIT Lincoln Laboratory, 244 Wood St Lexington MA 02420, AIAA Senior Member
[8] Associate Technical Staff, RF Technology Group, MIT Lincoln Laboratory, 244 Wood St. Lexington, MA 02420
[9] Technical staff, Applied Space Systems Group, MIT Lincoln Laboratory, 244 Wood Street, Lexington 02420, AIAA professional member

E-M	=	electromagetic
EM	=	expectation maximization
AKR	=	auroral kilometric radiation
RAE-2	=	Radio Astronomy Explorer-2
MWA	=	Murchison Widefield Array
LOFAR	=	Low Frequency Array
LWA	=	Long Wavelength Array
EMI	=	electromagnetic interference
RFI	=	radio frequency interference
DEVS	=	deployable electromagnetic vector sensor
LNA	=	low noise amplifier
1U	=	1 unit of a CubeSat (10 x 10 x 10 cm)
RAPID	=	Radio Array of Portable Interferometric Detectors
FPGA	=	field programmable gate array
θ	=	elevation spherical coordinate
φ	=	azimuth spherical coordinate
γ	=	polarization auxiliary angle
η	=	polarization phase difference
$\boldsymbol{y}$	=	vector sensor response
β	=	signal amplitude
$\boldsymbol{a}$	=	vector sensor steering vector
$\boldsymbol{n}$	=	white complex zero-mean Gaussian process
n	=	n^{th} time interval
m	=	m^{th} spacecraft in the interferometer
i	=	i^{th} source in the sky (or sky 'pixel' containing a white Gaussian process)
c_i	=	intensity of i^{th} source
$\boldsymbol{\tau_i}$	=	time delay for source i for each m satellite in the interferometric array
k	=	index for vector sensor elements (k=1:6)
$\boldsymbol{S}$	=	vector sensor data covariance matrix
$\boldsymbol{A}$	=	matrix of steering vectors (**a**) for every sky pixel
Σ	=	vector of estimates in the EM algorithm
$\boldsymbol{R}$	=	estimated covariance in the EM algorithm
$\boldsymbol{R_n}$	=	noise covariance matrix in the EM algorithm
Y_l^m	=	spherical harmonic function of degree l and order m
a_{lm}	=	spherical harmonic function scaling coefficient
$\boldsymbol{A_{sh}}$	=	steering vector matrix for integrated response to spherical harmonic components
Σ_{sh}	=	vector of estimated spherical harmonic coefficients

I. Introduction

The portion of the electromagnetic (E-M) spectrum below 10 MHz is poorly explored due to the opacity of the Earth's ionosphere below the local ionospheric plasma frequency (cut-off frequency). The plasma frequency of the ionospheric peak ranges from 5 to 15 MHz, depending on the time of day and ionospheric conditions. Ground-based observations in the range ~20 MHz to ~100 MHz, just above the ionospheric plasma frequency, are challenging due to increasing refraction and scattering, while observations below the ionospheric plasma are not possible from the ground. Low frequency, or long wavelength, science requires the ability to image the sky. At wavelengths on the order of meters, monolithic dish antennas are no longer feasible since they would need to be kilometers in diameter in order to obtain reasonable angular resolution. Interferometric arrays solve this problem by creating a synthetic aperature from widely spaced individual antennas. Ground-based low frequency observatories (MWA[1], LOFAR [2], LWA [3,4]) typically use individual crossed dipoles or small dipole phased arrays as the individual elements of an interferometric array.

In this paper, we propose a novel individual interferometric array element, the vector sensor, as an alternative to crossed dipoles or tripoles for a space-based array capable of imaging the sky below the ionospheric cut-off. We first describe the science objectives for low frequency radio astronomy (Section II), describe the vector sensor mathematically (Section III), and present two practical implementations of the vector sensor concept (Section IV), one for ground-based testing and one for space applications. We then describe novel imaging algorithms applied to

simulated and real data (Section VI) and ground-based measurements taken at frequencies above the ionospheric cut-off using a single vector sensor (Section VII).

II. Low Frequency Radio Astronomy

The desire for a low frequency observatory capable of observing below the ionospheric cut-off naturally suggests a space-based interferometric array located well above the ionospheric peak. Observations below 10 MHz would enable study and tracking of solar coronal mass ejections [5], solar system and exoplanetary auroral radio emission [6], mapping of the interplanetary and interstellar medium in the local neighborhood [7], investigations of galactic cosmic ray origins [8], galactic magnetic field mapping, energetic processes such as supernovae[9] and active galactic nuclei, and early universe studies including the Epoch of Reionization and the formation of the first stars [10]. A space-based low frequency observatory will require tens of spacecraft to achieve sufficient u-v plane coverage for sky mapping. Interferometry requires position knowledge (though not necessarily control) of each array element to a fraction of the operating wavelength (typically 1/10). For 30 MHz (λ = 10 m) observations, 1 m position knowledge is required.

To date, there has been only one space mission, RAE-2 [11,12], that was dedicated to mapping the sky below 10 MHz. Though several space-based low frequency observatories have been proposed [13–17], none have been selected for flight. The cost and complexity of constellations in space scale quickly with the number of spacecraft required. The design of the individual array element should therefore be optimized so that the total number of array elements can be minimized. We propose the vector sensor as an optimal array element that will reduce the total number of elements required by a factor of two when compared to tripole elements for a given sensitivity requirement. The vector sensor is a more complex single element than a triple (2x receive channels, etc.), but the reduction in required spacecraft justifies the added single element complexity.

The vector sensor described below is often referred to as the 'HF Vector Sensor' or 'HFVS', where HF refers to the 3 to 30 MHz frequency band. The ground-based version of the vector sensor (Atom) is optimized for this band, but the space-based antenna (DEVS) will operate from 300 kHz to 30 MHz, encompassing the HF band and the MF (300 kHz to 3 MHz) band.

III. Vector Sensing

To maximize the information gained in each node of that space-based array, we propose the use of a vector sensor as the fundamental antenna element of a future low frequency interferometric array. A vector sensor is composed of three orthogonal dipoles (a dipole triad) and three orthogonal loops (loop triad) with a common phase center. The six elements of the vector sensor enable independent measurement of the four spatial parameters that describe the propagation of an electromagnetic wave in space. The four parameters are two coordinate angles, in spherical coordinates used here, Θ and Φ, and two parameters that determining the polarization sense, ellipticity γ and η. The loops provide individual element patterns that are consistent with the response of a magnetic dipole. With the combination of the electric and magnetic dipole responses we characterize the vector sensor as measuring the E-field and B-field vectors of incoming radiation.

A single signal impinging on the vector sensor loops and dipoles is in the form of an amplitude-weighted array response vector. That is, the response of the array is

$$\mathbf{y} = \beta \mathbf{a}. \tag{1}$$

The vector **a** is the array response vector:

$$\mathbf{a} \equiv \mathbf{a}(\theta,\phi,\gamma,\eta) \equiv \begin{bmatrix} e_x \\ e_y \\ e_z \\ h_x \\ h_y \\ h_z \end{bmatrix} = \begin{bmatrix} \cos\phi\cos\theta & -\sin\phi \\ \sin\phi\cos\theta & \cos\phi \\ -\sin\theta & 0 \\ -\sin\phi & -\cos\phi\cos\theta \\ \cos\phi & -\sin\phi\cos\theta \\ 0 & \sin\theta \end{bmatrix} \begin{bmatrix} \sin\gamma\, e^{j\eta} \\ \cos\gamma \end{bmatrix} \tag{2}$$

Angle of Arrival (θ, ϕ), amplitude, β and polarization state (γ, η) are embedded in the array response through the steering vector **a.** This array response is originally from [18] and parameterizes polarization by auxiliary angle (γ) and phase difference (η).

The received data is a superposition of the sources from different angles and the received data is collected as a time series. We represent the totality of sources by the summation into received data vectors for each satellite.

The received data vector for the n^{th} time sample of N total samples for satellite m of M, denoted, $\mathbf{y}(n,m)$, is

$$\mathbf{y}(m,n) = \sum_{i=1}^{I} c_i(m,n)\,\mathbf{a}_i\,(m,n) + \mathbf{n}(m,n), \tag{3}$$

where the receiver noise, $\mathbf{n}(m,n)$, is a white complex zero-mean Gaussian process, $CN(0,\mathbf{R}_n)$. The $\mathbf{a}_i(m,n)$ are the steering vectors corresponding to the n^{th} time sample for the m^{th} satellite for the i^{th} source of I sources and the $c_i(m,n)$are the intensities of the sources. This particular formulation allows for arbitrary rotation of the individual satellites that has negligible motion during the period of each individual time sample

The formulation in Eqn. 1 can be applied to a spatially-distributed source where source is discretized into pixels, each pixel being modeled as one of the I sources. For problems of interest the propagation medium can be polarizing and the EMVS is polarization sensitive. As a result, we use two polarization bases, notionally either right and left circular, or horizontal and vertical linear to span the polarization space. We use a single index into the entire three-dimensional array. As a result, there will be *I* cells with discretization over both spatial angles and polarization state. In each source cell we assume radiation from a complex white Gaussian process.

We can further develop this model to provide a common galactic reference for the sources. First, as the vector antenna captures fully the electromagnetic field a local transformation of coordinates for the measured data at each time step can be performed such that the $\mathbf{a}_i(m,n)$ for each satellites are expressed in a common galactic reference system. As a rotation of coordinates, this transformation is a single transformation on $\mathbf{y}(m,n)$ and thus identical for all of the $\mathbf{a}_i$ for any particular satellite. Since the vector sensor responses are identical after calibration this transformation removes the dependency of the steering vectors on time and satellite; $\mathbf{a}_i = \mathbf{a}_i(m,n)$.

Secondly, the propagation of the sources across the constellation of satellites results in a time delay. Assuming the time delay across the satellite constellation is small relative to the inverse of the bandwidth the narrow-band approximation can be made [19] and with this approximation the time delay from element to element can be approximated as a phase shift and the amplitude of the time samples as being constant across the constellation of satellites, that is, $c_i(m,n) = c_i(n)e^{j\omega\tau_i(m)}$. The phase shift can be moved from the amplitude term and incorporated into an augmented array steering vector

$$\tilde{\mathbf{a}}_i = \begin{bmatrix} \mathbf{a}_i e^{j\omega\tau_i(1)} \\ \vdots \\ \mathbf{a}_i e^{j\omega\tau_i(M)} \end{bmatrix} = \boldsymbol{\tau}_i \otimes \mathbf{a}_i \tag{4}$$

with the vector $\boldsymbol{\tau}_i = [e^{j\omega\tau_i(1)} \cdots e^{j\omega\tau_i(M)}]$. The full data matrix, can then be expressed in matrix vector form as:

$$\mathbf{Y} \equiv \begin{bmatrix} \mathbf{y}(1,1) \cdots \mathbf{y}(1,N) \\ \vdots \\ \mathbf{y}(M,1) \cdots \mathbf{y}(M,N) \end{bmatrix} = \tilde{\mathbf{A}}\mathbf{C} + \mathbf{N}. \tag{5}$$

In this expression, $\tilde{\mathbf{A}} = [\tilde{\mathbf{a}}_1 \quad \cdots \quad \tilde{\mathbf{a}}_I]$ and the rows of $\mathbf{C}$ are the time series corresponding to each of the sources. The receiver noise $\mathbf{N}$ has been transformed as well. Since receiver noise is typically a multiple of the identity matrix and the coordinate rotation can be performed as a unitary transformation, the covariance structure of the noise can be preserved.

This formulation of the data model forms the basis of our estimation algorithms.

Using vector antenna is a significant departure from the crossed dipoles or dipole triads that have been proposed previously for space-based low frequency interferometric arrays. The increase in complexity is justified by the increase in per-satellite sensitivity that the vector sensor provides, particularly in the presence of interfering signals such as man-made RFI or Earth's auroral kilometric radiation (AKR). An interferometric array composed of vector sensors will reduce the total number of array nodes needed by at least a factor of two for a given sensitivity level.

IV. HF Vector Sensor Implementation

A. ATOM antenna

A rugged electromagnetic vector sensor for ground-test use in the HF band (3 to 30 MHz) has been implemented based on the design of Meloling et. al. [20]. The ground-based vector sensor antenna in Figure 1 consists of three orthogonal loops, each with 1 m diameter. To ease mechanical fabrication, each loop is approximated by using straight sections of 2.22 cm (0.875 inch) OD copper tubing and 45° copper elbows that form an octagon. The

orientation of the three loops is such that corresponding segments at the bottom of the vector sensor antenna are located in a plane parallel to the ground. Each loop has two feed terminals located at opposing points on the octagon. By phasing the two feed terminals with a sum and difference hybrid the current flow on the octagon generates both short dipole and uniform current loop receive antenna modes [21]. The full antenna produces the six output channels (three dipole antenna modes and three loop antenna modes) consistent with measuring each component of the electromagnetic field, referenced to the orientation planes of the three loops. To achieve balanced antenna feeds, transformer baluns are mounted within the copper tubing, and the transformer leads are connected to the antenna terminals. Flexible coaxial cables are routed inside the copper tubing from the antenna terminals to the vector sensor modeformer. Machined Delrin blocks are used to connect and support the painted copper tubing. The vector sensor antenna is supported approximately 2 m above the ground by three adjustable PVC legs.

Figure 1. Atom 1 vector antenna at MIT Haystack Observatory. The three octagonal loops that form the vector sensor are white-painted copper tubing and the support posts are PVC. Each loop is 1 m in diameter.

B. Amplifier

A key aspect of the instrumentation system is the front end amplifier. This has been described in previous publications [22]. For the ground-based observations we supplied very well regulated, electrically clean power over the coaxial cable used to carry the RF signals. Extra care was used to provide very clean power from a low noise secondarily regulated supply and from a battery sourced supply.

To compensate for the impedance characteristics of the ATOM antenna, a novel active mode forming amplifer was constructed. Traditional Foster-type matching is impossible to achieve with wide bandwidth given the antenna impedance, and the two modes have conflicting amplification requirements. Therefore, the unbalanced feeds from the split loops of the ATOM antenna are connected to a hybrid transformer to separate the modes before amplification by circuitry specifically tailored to the electrical models of the modes.

The loop mode consists of a voltage source in series with an inductance. Since effective height of a loop increases with frequency, this voltage increases with frequency. This is counteracted by the increasing reactance of the inductor, resulting in constant current over frequency. It naturally follows that a transimpedance amplifier would be the correct solution. This amplifier holds its input at virtual ground, thus negating the effect of parasitic capacitance. Common gate current buffers are used at the input of this amplifier to avoid noise gain peaking due to the antenna's low impedance effectively negating the amplifier's feedback path.

The dipole mode consists of a voltage source in series with a small capacitance. The voltage will remain constant over frequency due to the effective height being constant. Since this capacitance is very small, any parasitic capacitance will act as a voltage divider. Again, it naturally follows that a charge amplifier with current buffers is the correct solution to negate the effect of parasitic capacitance and provide flat gain over frequency [23,24].

Power was provided to the low noise amplifiers using a power supply or an external LiFePO battery in some cases where we attempted to minimize the noise present at the LNA power input.

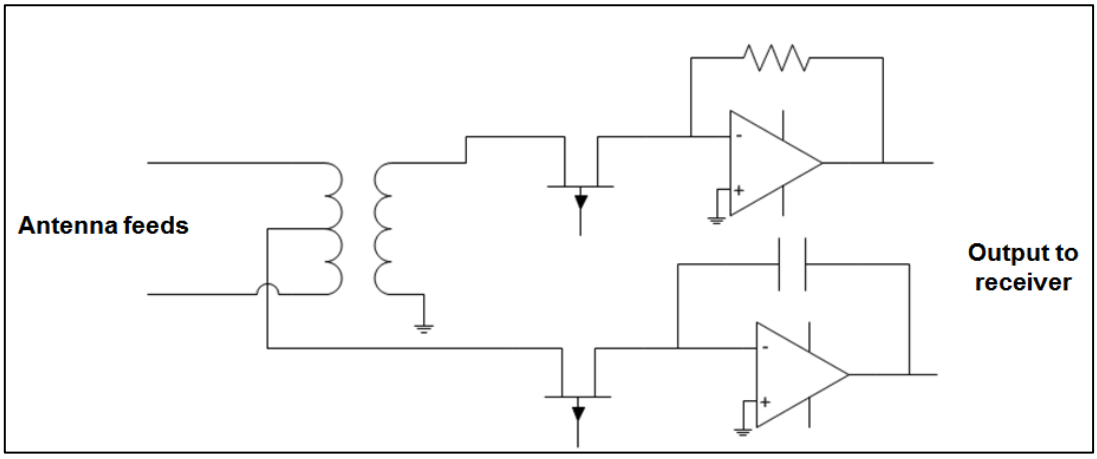

Figure 2. Atom LNA schematic

Initial ground testing of the vector sensor antenna is in progress at MIT Haystack Observatory in Westford, MA. An initial test was the detection and mapping of the NIST WWV 15 MHz transmission[22]. Figure 3 illustrates an image produced from the measured data of the six vector sensor antenna elements using an equal area discretization on the sphere [25] and the maximum-likelihood estimation algorithm [26]. The results presented here indicate that the ground-based vector sensor is able to localize bright sources.

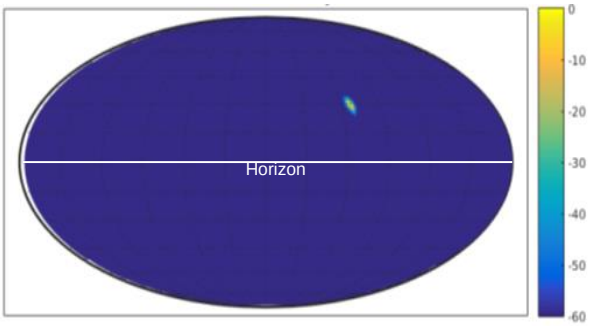

Figure 3. Example of direction finding for reception of the WWV[34] radio transmissions at 15 MHz. The source map coordinates are local elevation and azimuth, with 0 degrees in elevation, the local horizon, marked by the white line. The color indicates the Stokes intensity, I, in dB.

C. Deployable Electromagnetic Vector Sensor (DEVS)

The Atom antenna is well suited to ground-based testing and development, but the science applications discussed in Section II require a space-based sensor. DEVS is a vector sensor configuration that can be rolled up and stowed into a small volume for satellite applications. This configuration consists of 4 vertical loops, a horizontal loop and a vertical monopole (see Figure 4). A deployment testbed was developed for DEVS to investigate how a 4 meter diagonal version of the the sensor might stow and deploy from a 1U CubeSat (10 cm x 10 cm x 10 cm) form factor. The vertical loops are made from steel carpenters tapes, the horizontal loop is made out of wire and the vertical monopole is another steel carpenters tape. The tapes are used as the conducting antenna elements and they also serve as the structural members forming the shape of the antenna.

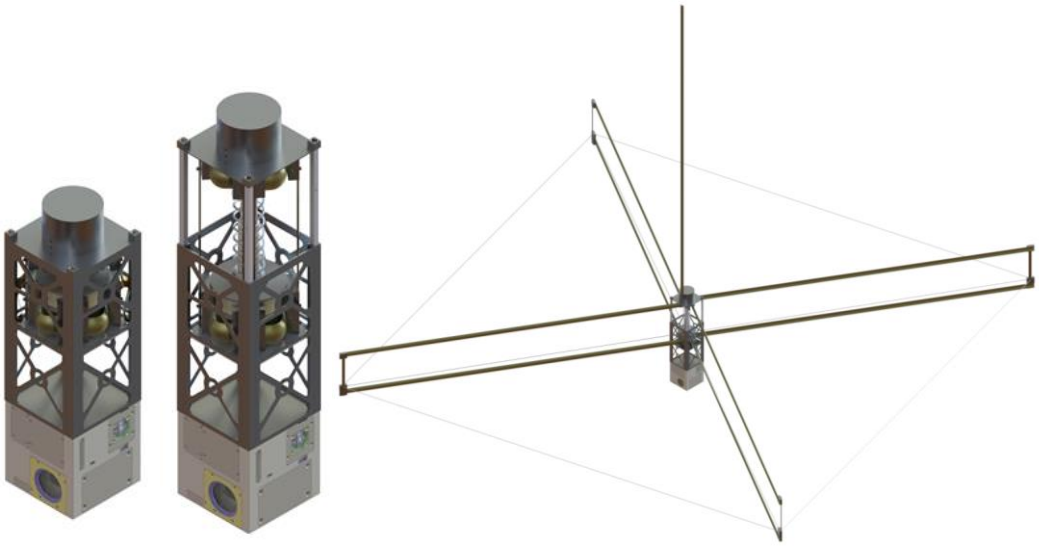

(a) **(b)** **(c)**

Figure 4. DEVS antenna fully stowed (a), telescoped but not deployed (b), and fully deployed (c). The vertical monopole is stowed in the cylinder on the top of the 3U CubeSat frame and the remaining five elements (two rectangular loop/dipoles and square perimeter loop) are stowed in the top 1U.

For this deployment testbed, the antenna stow process begins with coiling the radial portion of the vertical loops and horizontal loops around a central telescoping tube. This is done by spinning the central telescoping tube about its axis. The action of rolling up the steel carpenters tapes provides stored strain energy which later drives the deployment of the antenna when they are release.Then, the vertical portions of the vertical loops are collapsed along with the spring loaded central telescoping tube to fit into the 1U form factor. The vertical monopole can be rolled up to fit within the available volume in the center of the central telescoping tube. The vertical members of the vertical loops are also steel carpenters tapes. The radial and vertical members of the vertical loops are riveted and soldered at the joints to ensure good electrical conductivity.

In order to investigate the deployment in Earth's gravity, a gravity offload frame was built to keep the steel carpenters tapes from collapsing under their own weight during the deployment. Only the tips of the vertical loops are attached to a low friction sliding rail on the offload frame (Figure 5). This limited the loops length to 1.5 m (3 m tip-to-tip) for the testbed because beyond that length the gravity load in the center of the radial portion of the vertical loops was enough to cause the tapes to fold and drop towards the ground.

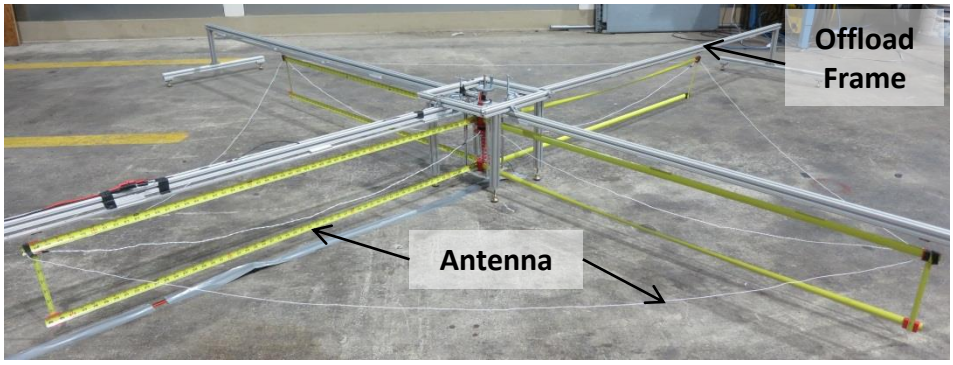

Figure 5. DEVS deployed in gravity offload frame. The vertical monopole was not included in this deployment test.

The deployment sequence was tested several times and was very repeatable. The deployment was initiated by using nichrome wire to burn through a nylon string that held the spring loaded telescoping tube collapsed. This released the telescoping action and deployed the vertical portion of the vertical loops to their full height. Then, a second nichrome wire was heated to burn through a nylon string releasing the rolled steel carpenters tapes. The stored strain energy in the rolled steel carpenters tapes is enough to drive the deployment of the vertical loops in addition to pulling out the wires making up the horizontal loops.

This DEVS deployment testbed showed that the concept is feasible. However, after this testing was completed several alternative carpenter tape materials and stow/deploy configurations have been considered to provide a more lightweight and robust deployable antenna system. The design and testing of the DEVS antenna as well as a high altitude balloon test are described in more detail in [22].

V. Data Acquisition System

A. Receiver

Figure 6. Low EMI receiver box containing Ettus receiver, filters, power supplies, GPS stabilized oscillator, and solid state disks for data recording.

Ground based data acquisition has been performed using commercial Ettus N200 radios with basic RX receiver boards integrated into a customized low EMI enclosure. See Figure 6. A radio, data acquisition computer, GPS stabilized oscillator, and solid state storage are combined in the enclosure to enable portability. These systems were originally developed as hardware prototypes for the RAPID project [27] and have corresponding solar and battery power units for cases where field operations are required. Three separate receivers were used to help isolate the independent channels of the vector sensor and to prevent self interference that was observed when using multiple software radios in the same enclosure. External synchronization to a common external reference clock was used for most experiments to ensure that the software radios were stable in time and frequency.

A custom FPGA firmware was implemented for the Ettus N200 receivers to address performance issues with low signal levels and low sampling bandwidths. The first issue, identified in initial data collections with low signal levels, was a DC bias on the order of 20 dB above the receiver noise floor. It was determined that this bias was a result of truncation applied in the FPGA to reduce the bit depth after filtering. Replacing the truncation with rounding removed the bias, and this fix has since been included in the commercial FPGA code release. The second issue occurred in collections with low sampling bandwidths and presented as a valley in the noise floor around the center frequency. It was discovered that this noise shaping is by design in order to reduce quantization noise around the center frequency, and it is evident only when quantization noise is the dominant noise source as happens with high decimation rates. In order to reduce quantization noise in the low bandwidth regime, a variable bit scaling was implemented in the N200's FPGA. The scaling provides a digital gain that keeps low-order bits acquired from decimation at the expense of high-order bits that are unused when the signal level is low.

B. Data Recording

Data recording uses the DigitalRF data format which implements raw voltage capture in the HDF5 data format. Acquisition bandwidth was limited by the available data storage and for some experiments external computers were used to obtain data from each of the receivers over Ethernet connection. Recording bandwidth was limited by data storage capacity and the overall capability of the Ettus radios (dual channel) to at most 15 MHz per channel which could be tuned in center frequency using the N200 digital downconverter. In most cases a more narrow acquisition was used to extend the observation time possible for a given experiment. Figure 7(left) shows an extended data collection using a terminator to evaluate system self noise and (right) shows a similar collection using an injected noise diode. Amplitude stability in the receiver was more variable when low bit depths were being excited at the A/D convernter input. Short term variability with the injected diode was on the order of 0.02 dB while longer term variations were on the order of 0.15 dB. Terminated inputs show about an order of magnitude higher variation and some residual spectral content in time and frequency can be seen. The data acquisition system also exhibits temperature dependence that we have not quantified directly.

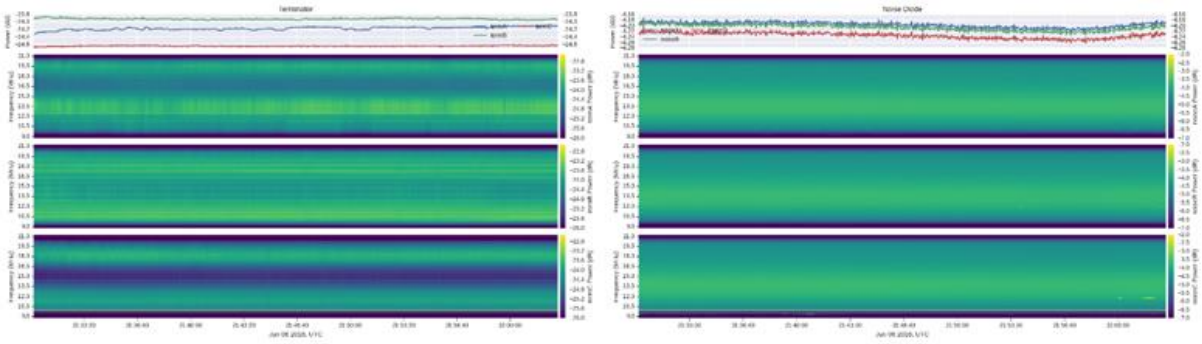

Figure 7. Signal power versus time and frequency for terminated receiver inputs (left) and for a noise diode (right). Power versus time is shown at the top and the different amplitude scales used to highlight the relative variability should be noted.

C. Noise Mitigation

Noise due issues at different field test sites and self noise of the data acquisition systems proved to be early impediments to successful data acquisition. Self noise was particularly important and included significant conducted signals in the HF band from the system DC/DC converters, cross-interference between radios, Ethernet switch interference when attempting to use three radios in one enclosure, externally noise conducted over power lines, and noise radiating from the GPS synchronized oscillator. These issues were systematically addressed as they were discovered. In particular, a low EMI power supply was implemented to resolve noise issues from the DC/DC switching power converters used to power the radio. The result of this modification is show in Figure 8 where the left panel shows a noisy commercial DC/DC converter measured at the power supply input to the radio and the right panel shows the custom low EMI DC/DC converter. Most of the spectral response visible in the low noise supply measurement is from the surrounding laboratory environment (determined by measuring with the supply off; not shown). Note these are conducted emissions at the power supply input prior to on radio regulation and filtering. In practice the noisey DC/DC converter produced significant signals in the collected data and proved unusable.

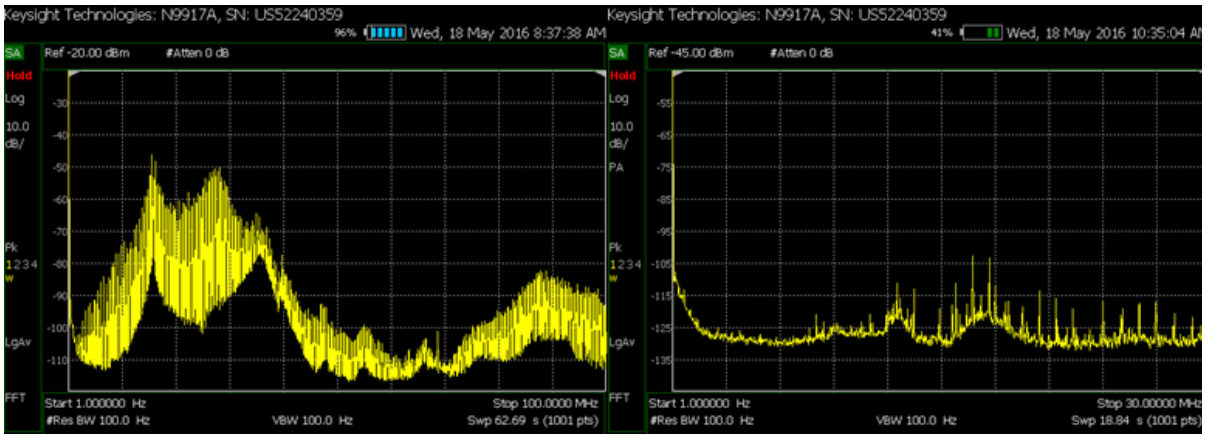

Figure 8. Spectral analyzer measurements of conducted emissions in the at the power supply input to the software radio with a 2A controlled load. The measurements show a noisy DC / DC converter (left) and a low EMI DC/DC converter (right). The low frequency response and spectral lines observed on the right are due to the analyzer and from the local environment respectively. A pre-amplifier was also used for the low EMI converter measurements.

VI. Imaging Algorithms

A. Expectation Maximization

The application of the expectation maximization (EM) algorithm to vector sensor imaging is described in detail in [26], [28] and references therein. Briefly, we represent the vector sensor data by a K x N matrix, where temporal samples are indexed by n and vector sensor elements are indexed by k (k=1…6). The sky is represented as I angular

resolution elements, each with a complex white Gaussian process generating radiation. Polarization is represented by either a right and left circular basis or a linear vertical and horizontal basis. As described in Section III, the data received by the vector sensor, *y*, at temporal index *n* is represented by

$$y[n] = \sum_{i=1}^{I} c_i[n]\boldsymbol{a_i} + n[n], \tag{6}$$

where $\boldsymbol{a_i}$ is the steering vector associated with direction *i*, c_i is the result of the complex white Gaussian process at that location, and *n* is the receiver noise, a white complex zero-mean Gaussian process. In matrix form,

$$\boldsymbol{Y} = \boldsymbol{AC} + \boldsymbol{N}$$

We estimate a set of parameters that represent either resolution elements on the sky (i.e. 'pixels') or coefficients of spherical harmonics. Other parameter choices are possible, but not discussed here.

The steps of the EM algorithm are as follows:

1. Initialize the complete spectral data estimates Σ^1 and covariance matrix

$$\widehat{\boldsymbol{R}}^1 = \boldsymbol{A}\hat{\Sigma}^1\boldsymbol{A}^H + \boldsymbol{R}_n \tag{7}$$

2. Integrate the following for $p = 1 \ldots P$:

$$\Sigma^{p+1} = diag(\Sigma^p + \hat{\Sigma}^p\boldsymbol{A}^H\left(\hat{R}^{p^{-1}}\boldsymbol{S}\widehat{\boldsymbol{R}}^{p^{-1}} - \widehat{\boldsymbol{R}}^{p^{-1}}\right)\boldsymbol{A}\hat{\Sigma}^p \tag{8}$$

$$\widehat{\boldsymbol{R}}^{p+1} = \boldsymbol{A}\Sigma^{p+1}\boldsymbol{A}^H + \boldsymbol{R}_n \tag{9}$$

where *A* is the steering vector matrix and S is the sample covariance matrix:

$$\boldsymbol{S} = \frac{1}{N}\boldsymbol{YY^H} \tag{10}$$

This estimation formulation is used for both approaches below.

B. Pixel-based Approach

As described above, the sky map can be represented as a set of resolution elements or pixels. At each pixel location, there are actually two pixels. The two pixels represent the two parts of the polarization basis, either right and left circular or vertical and horizontal. The combination of these two pixels spans all possible polarization states. HEALpix [25] was used to select pixel centers on the full 4π steradian sphere in order to avoid oversampling at the poles. The pixel-based approach fits naturally with the data model described above, and returns an estimate for each input pixel.

The pixel-based EM imaging approach yielded good results both in simulation (Figure 9) and with real data (Figure 3, Figure 14). It is currently the standard imaging algorithm ground-based testing of the vector sensor. The resulting images are necessarily non-unique, however, because the parameters needed to represent all pixels and polarizations far exceeds the constraints provided by the data. Non-unique imaging techniques for radio data are common and accepted in the radio astronomy community. The standard imaging algorithm for interferometric data, CLEAN [29], is routinely used to estimate many more parameters (pixels, polarization) than can be constrained by the data. Images resulting from CLEAN therefore vary depending on the parameters chosen for the algorithm.

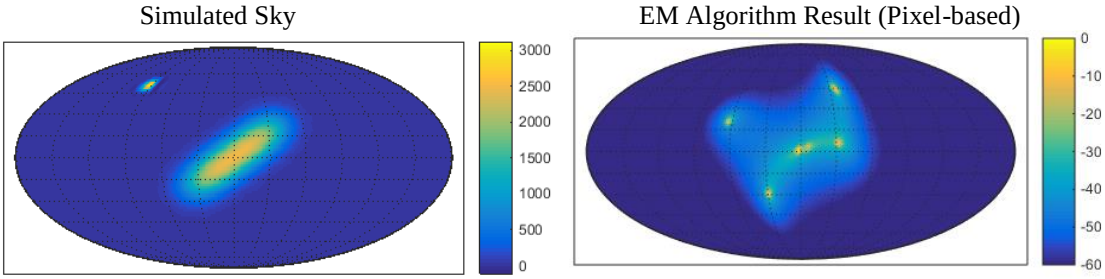

Figure 9. Simulated sky (left) and resulting estimate (right) using the expectation-maximization (EM) algorithm and estimating individual pixels.

The pixel-based approach is useful for identifying the brightest point-like sources in the sky. These may be interferers, such as transmitters, natural terrestrial emission, such as the auroral kilometric radiation (AKR) or lightning, solar or jovian bursts, or extremely bright astrophysical emitters (e.g. Cyg A, Cas A). Depending on the intent of the observation, the pixel-based approach may be used on its own if the object of interest is one of the

bright emitters listed above. Alternatively, it may be used to determine the direction of arrival, intensity, and polarization of unwanted flux so that it may be removed via nulling.

C. Spherical Harmonic Approach

An alternative approach uses a spherical harmonic expansion to approximate the brightness distribution of the sky. Spherical harmonics are a logical choice to represent the sky particularly in the case where the vector sensor is in space and is sensitive to the full 4π steradian celestial sphere. Estimating the coefficients of spherical harmonics, truncated at some relatively low degree l and order m, will bias the resulting image toward the spatially distributed emission present.

Spherical harmonic estimation techniques has been proposed for radio sky imaging [30,31], but these approaches are designed to operate in the visibility domain of radio interferometric measurements. In the single vector sensor case, the expectation maximization algorithm will be used to estimate n coefficients of spherical harmonic functions up to a pre-determined limit in l and m. If that limit is chosen such that the number of estimated coefficients is less than the available degrees of freedom, the resulting solution will be unique. The vector sensor has 19 degrees of freedom instantaneously (Ref. 26), so up to 19 coefficients may be estimated uniquely for a single observation using this approach. This yields a very low resolution map, ~l=3. Higher degree estimates are possible by several methods, including adding spatially separated sensors (interferometry), or pre-selecting only the spherical harmonic components that are expected to contribute significantly. The second approach introduces a model-based bias to the estimation.

The Haslam et.al. full sky map at 408 MHz [32], post-processed and prepared in HEALPix format [33], was used as input for simulating the spherical harmonic estimation approach. The full resolution map (~56 arcmin resolution) is shown in Figure 10, along with a version of the map represented by spherical harmonics up to degree l=3 (left) and l=20 (right). Even in the low degree map, the galactic plane and central galactic bulge are apparent.

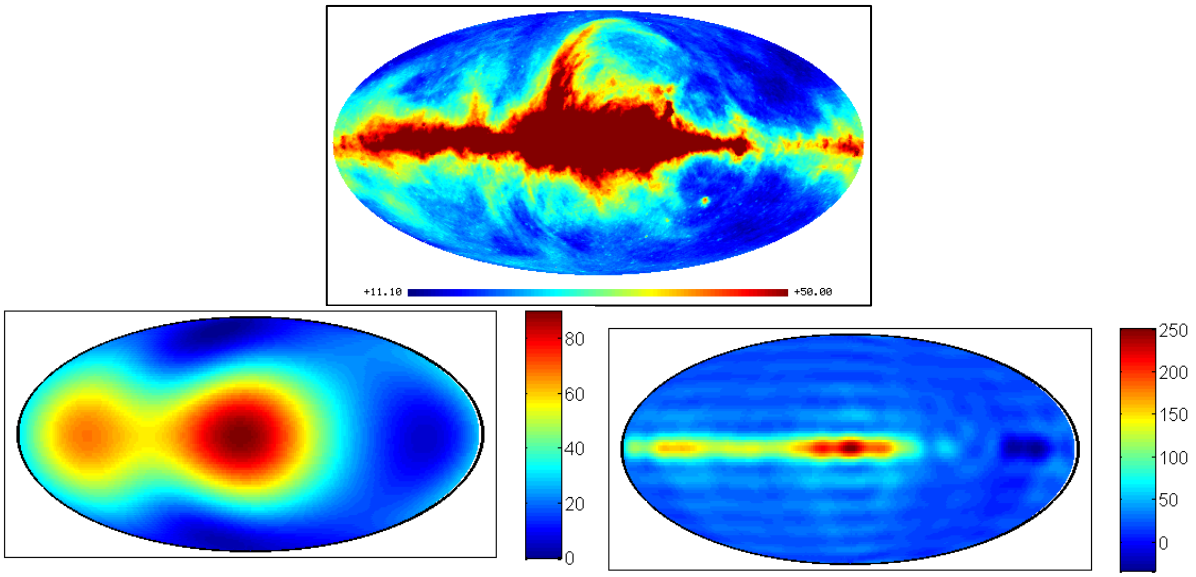

Figure 10. The post-processed Haslam et. al. map [33] (top center), the Haslam et. al. map represented by spherical harmonics to degree l=3 (bottom left) and degree l=20 (bottom right). There are some projection distortions at the edges of all the maps.

The l=0 term, or the global 'DC' flux level, can be estimated separately from higher degree terms. Estimating coefficients for all m ($-l \geq m \geq l$), there are 15 coefficients to l=3 and 24 to l=4 (not including l=0). There are therefore three possibilities when choosing which coefficients to estimate: 1) estimate all coefficients from l=1 to l=3 (15) for a unique solution, 2) estimate all coefficients from l=1 to l=4 for a higher resolution but non-unique solution, or 3) estimate coefficients from l=1 to l=4 while dropping some l=4 coefficients to estimate exactly 19 terms, yielding a unique solution.

The simplest way to proceed with spherical harmonic coefficient estimation using vector sensor data is to alter the content of the $\boldsymbol{A}$ and Σ terms in the EM equation (Eqns. 7-9) must be adapted to the spherical harmonic approach. The vector of estimates, Σ, is no longer a set of values corresponding to a resolution element ('pixel')

centered at (θ, φ). Instead, Σ becomes Σ_{sh}, a vector of spherical harmonic coefficients a_{lm}. $\boldsymbol{A}$ must be recast so that it represents the integrated vector sensor response to one spherical harmonic component. That means that $\boldsymbol{A_{sh}}_l^m$ is the response of the vector sensor to a particular Y_l^m integrated over all θ and φ. The real spherical harmonic Y_l^m is used for this calculation. For example:

$$\boldsymbol{A_{sh}}_l^m(k,s) = \int_0^{\pi}\int_0^{2\pi} \boldsymbol{a}(k)\cdot Y_l^m(\theta,\varphi)\,d\varphi\,d\theta \tag{11}$$

where k represents the vector sensor element index and s is the spherical harmonic component index. The result will be a function of the two polarization angles, γ and η. The resulting k x s matrix, $\boldsymbol{A_{sh}}$, replaces $\boldsymbol{A}$ in the EM algorithm. Table 1 shows $\boldsymbol{A_{sh}}$ for $l=1$.

Table 1. Example results for *l=1* of the vector sensor integrated response to a spherical harmonic component.

$\boldsymbol{A_{sh}}_1^{-1}$	$\boldsymbol{A_{sh}}_1^{0}$	$\boldsymbol{A_{sh}}_1^{1}$
$\begin{pmatrix} \sqrt{3\pi}\cos\gamma \\ 0 \\ 0 \\ e^{i\eta}\sqrt{3\pi}\sin\gamma \\ 0 \\ 0 \end{pmatrix}$	$\begin{pmatrix} 0 \\ 0 \\ 0 \\ 0 \\ 0 \\ 0 \end{pmatrix}$	$\begin{pmatrix} 0 \\ -\sqrt{3\pi}\cos\gamma \\ 0 \\ 0 \\ e^{i\eta}\sqrt{3\pi}\sin\gamma \\ 0 \end{pmatrix}$

Calculating the columns of $\boldsymbol{A_{sh}}$ up to $l=4$ reveals an interesting pattern. The only columns that have non-zero entries correspond to order $m=\pm1$. This is likely due to the symmetry of the sensor and the symmetry of the spherical harmonic functions. Unfortunately, this feature reduces the utility of this estimation method since analysis of real sky data indicates that there are significant non-zero coefficients for all degrees and orders. The problem needs to be reformulated to avoid this symmetry-induced degeneracy. That work is currently ongoing. The pixel-based estimation is the standard imaging tool for vector sensor data at this point.

Polarization can be handled in a similar manner to the pixel-based method. The spherical harmonic coefficients can be calculated separately for the four Stokes parameters (I, Q, U, V). Making four separate estimates of the spherical harmonic coefficients in order to fully specify the polarization state over the full sky will reduce the maximum degrees (l) available for the estimate, assuming a unique estimation is desired. More degrees may be added at the cost of a nonunique estimate of the coefficients. Other polarization estimation techniques are also being investigated.

VII. Ground-Based Observations and Results

A. 24+ hour Collection

One of our first experiments to test the ATOM antenna and receiver system was a low bandwidth, long duration collection to examine its sensitivity to astronomical radio sources. We deployed the antenna at a relatively radio quiet location near Barre, MA and set out to observe the noise floor in a quiet radio band with the hope of observing diurnal variations that could be attributed to the rise and set of the Sun or galactic center. We collected about 29 hours of data starting on March 31, 2016 with a 200 kHz bandwidth centered around 26 MHz. In order to compare with a resonant antenna and the receiver noise floor, we acquired data for two each of the dipole and loop modes of the ATOM antenna, an HF vertical antenna, and a 50 Ohm terminated input.

Results are shown in Figure 11and Figure 12, which depict the power observed over the course of the data

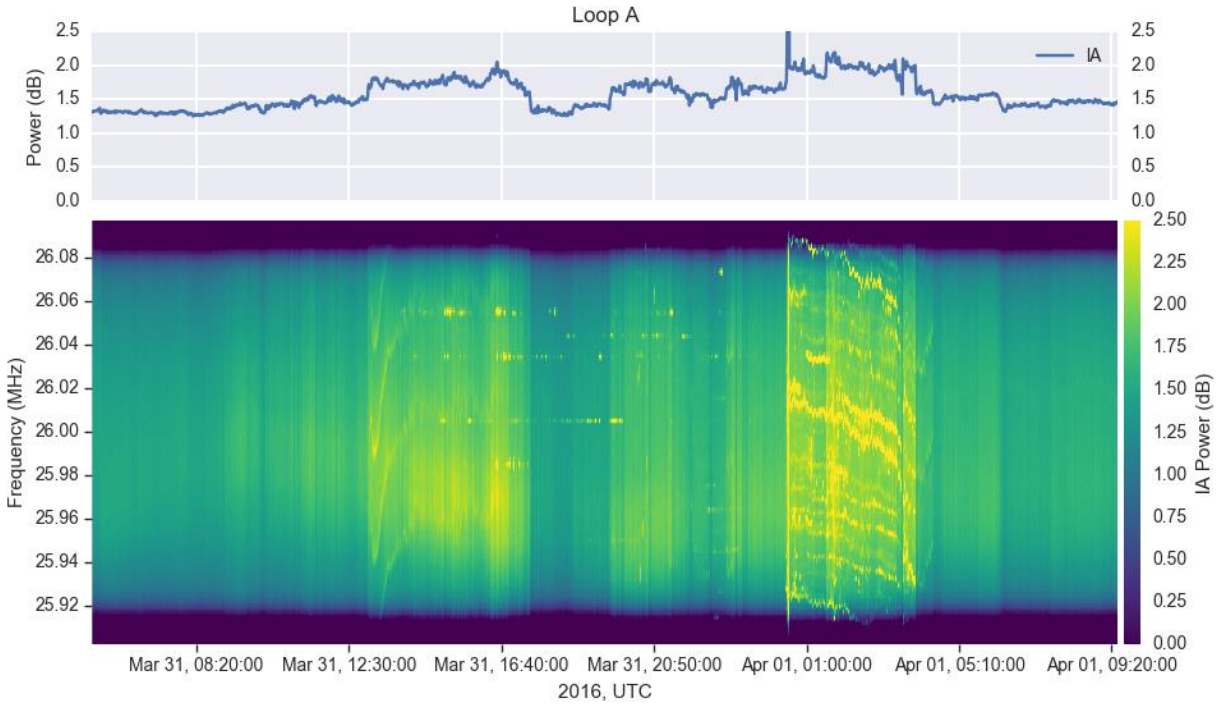

Figure 11. Median power (above) and spectrogram (below) for the Atom antenna's loop A channel during the long duration data collection. The background noise is interrupted by two primary periods of broadband interference from an unknown source.

collection. Despite the relatively remote location, the experiment suffered from significant RFI from an unknown source. The lower, stable power level of the terminated input shows that the signal channels are not receiver noise limited. The wildly varying power levels in all of the signal channels, including the resonant HF vertical, point toward RF interference as the dominant factor. The worst of this interference is evident in two separate time periods that exhibit power levels significantly above the background noise level. Unfortunately, because of the RFI, there is no discernable diurnal trend that can be attributed to astronomical noise sources.

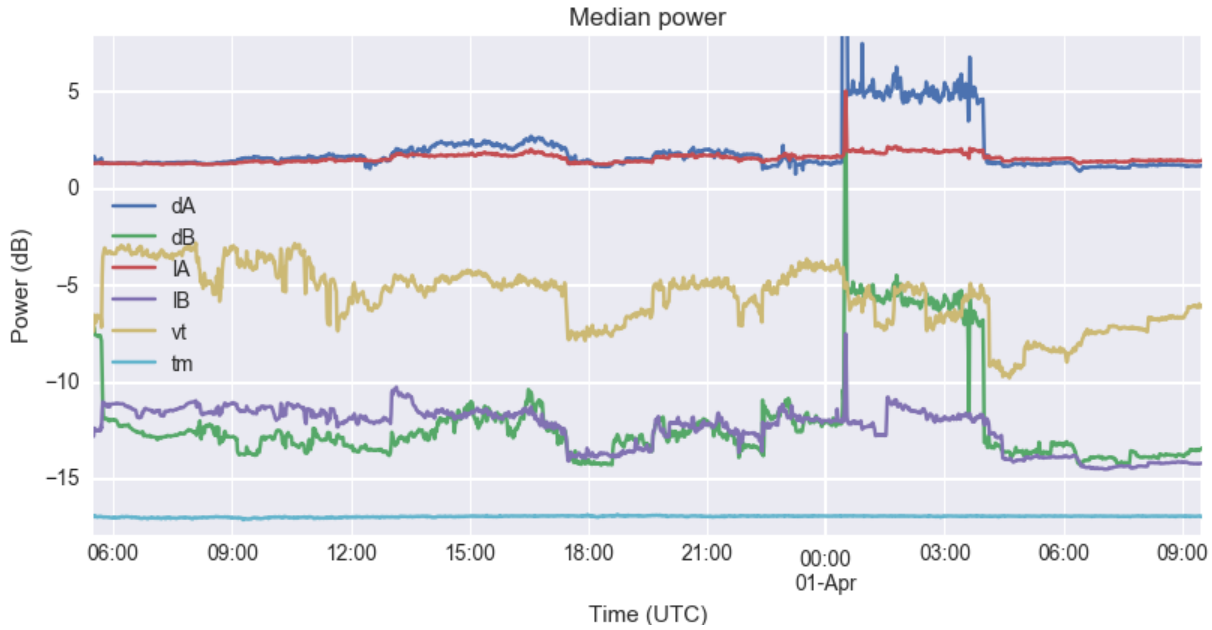

Figure 12. Median power for all six channels during the long duration data collection. The channels consisted of two of the ATOM antenna's dipoles (dA, dB), two of its loops (lA, lB), an HF vertical antenna (vt), and a terminated input (tm). No diurnal trend is evident due to the presence of RF interference.

B. Solar Burst Observation

Having concluded that the ATOM antenna in its current configuration and location was not sensitive enough to observe persistent astronomical radio sources, we turned our eye toward solar radio bursts as a potentially bright but transient astronomical source. Our strategy was to collect data for a couple of hours every day while the Sun was overhead and analyze the data afterward looking for solar activity. Fortunately, a period of high solar activity presented itself and we were able to collect data on July 21, 2016 that coincided with a NOAA-reported solar radio burst event at 245 MHz. The spectrograms from this event are shown in Figure 13. They depict four broadband spikes, each lasting a few seconds and ocurring in a span of under a minute, that represent our suspected solar radio burst. All-sky maps of Stokes components estimated using the pixel-based EM imaging algorithm applied to the first spike is shown in Figure 14. The maps show signal coming from two directions, one in the Northern hemisphere and one in the Southern hemisphere. The Northern source has approximately the correct elevation for a solar signal at that location and time of day, but its azimuth is offset from where one would expect. The source in the Southern hemisphere is opposite the Northern hemisphere source, so it most likely represents a ground image of the true source. These results are encouraging and point toward the desired capabilities of the vector sensor, but further calibration is needed to ensure accuracy and prove the direction-finding technique.

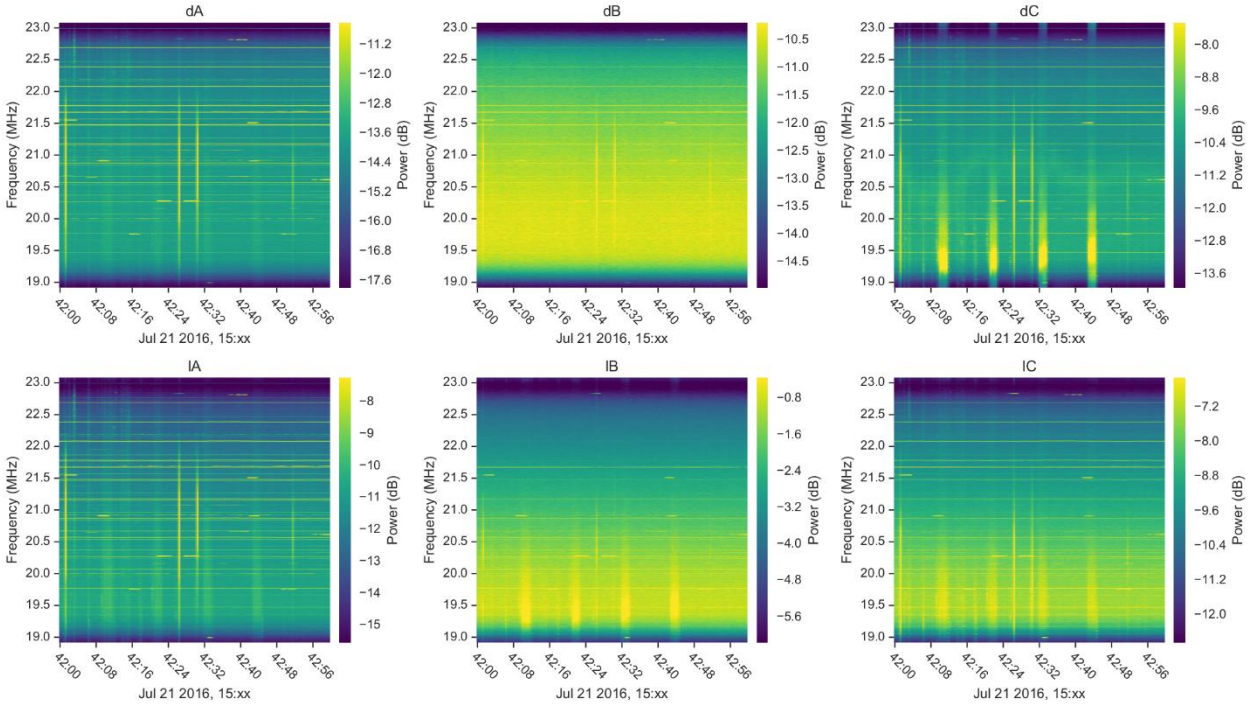

Figure 13. Spectrograms from all six vector sensor channels (dipoles A, B, C and loops A, B, C) showing potential solar radio burst detections. Four broadband spikes, each lasting a few seconds, coincide with a NOAA-reported solar radio burst event at higher frequencies.

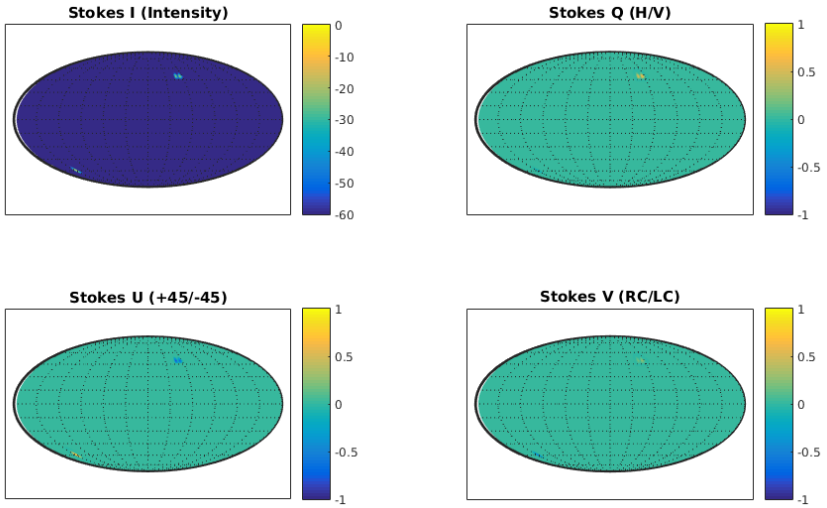

Figure 14. Sky map of the measured solar radio burst generated by the vector sensor imaging algorithm. Each map is a Mollweide projection with zenith at the top and the horizon across the widest part of the map. The source in the Northern hemisphere has approximately the correct elevation for a solar source, but its azimuth is offset. A ground image appears in the Southern hemisphere. Further calibration is needed to refine the direction-finding capabilities of the vector sensor.

VIII. Conclusion

Two vector sensor designs, one for ground-based observation and one for space applications, were presented. The vector sensor is a highly capable individual instrument, allowing for direction of arrival, flux, and polarization estimation of multiple sources in a single snapshot. Limited sky mapping is possible with a single vector sensor. The

additional degrees of freedom of the vector sensor also recommend it as a highly capable interferometric array element. Vector sensors may be an enabling technology for a future space-based low frequency interferometric array.

We have developed two imaging approaches for vector sensor data. The Atom antenna and custom LNA were used with custom low EMI data acquisition equipment to collect data at a local field site. We applied both imaging approaches to ground-based onbservations successfully. RFI/EMI mitigation is a major challenge at HF/MF frequencies, and will be key to designing a successful space-based system to probe the last frontier of the EM spectrum.

Future work with the vector sensor will focus on three key areas: 1) designing compact, space-qualified, low EMI electronics for the DEVS, 2) demonstrating the interferometric capabilities of the vector sensor, and 3) further refining and improving imaging and nulling algorithms.

Acknowledgments

We would like to thank the Lincoln Laboratory Advanced Concepts Committee for financial support of the HFVS development and testing. We also thank Will Rogers and Tom Brown of MIT Haystack Observatory for their help in receiver system integration, receiver testing, field experiment setup, and data acquisition.

References

[1] Lonsdale, C. J., Cappallo, R. J., Morales, M. F., Briggs, F. H., Benkevitch, L., Bowman, J. D., Bunton, J. D., Burns, S., Corey, B. E., deSouza, L., Doeleman, S. S., Derome, M., Deshpande, A., Gopala, M. R., Greenhill, L. J., Herne, D. E., Hewitt, J. N., Kamini, P. A., Kasper, J. C., Kincaid, B. B., Kocz, J., Kowald, E., Kratzenberg, E., Kumar, D., Lynch, M. J., Madhavi, S., Matejek, M., Mitchell, D. A., Morgan, E., Oberoi, D., Ord, S., Pathikulangara, J., Prabu, T., Rogers, A., Roshi, A., Salah, J. E., Sault, R. J., Shankar, N. U., Srivani, K. S., Stevens, J., Tingay, S., Vaccarella, A., Waterson, M., Wayth, R. B., Webster, R. L., Whitney, A. R., Williams, A., and Williams, C., "The Murchison Widefield Array: Design Overview," *Proceedings of the IEEE*, vol. 97, Aug. 2009, pp. 1497–1506.

[2] De Vos, M., Gunst, A. W., and Nijboer, R., "The LOFAR telescope: System architecture and signal processing," *Proceedings of the IEEE*, vol. 97, 2009, pp. 1431–1437.

[3] Ellingson, S. W., Clarke, T. E., Cohen, A., Craig, J., Kassim, N. E., Pihlstrom, Y., Richard, L. J., and Taylor, G. B., "The Long Wavelength Array," *Proceedings of the IEEE* Available: http://lwa.phys.unm.edu/docs/lwa0157.pdf.

[4] Hallinan, G., "The Owens Valley LWA," *Exascale Radio Astronomy*, 2014.

[5] Warmuth, A., and Mann, G., "The Application of Radio Diagnostics to the Study of the Solar Drivers of Space Weather," vol. 70, 2005, pp. 51–70.

[6] Zarka, P., Treumann, R. A., Ryabov, B. P., and Ryabov, V. B., "Magnetically-Driven Planetary Radio Emissions and Application to Extrasolar Planets," *Astrophysics and Space Science*, 2001, pp. 293–300.

[7] Linfield, R. P., "IPM and ISM Coherence and Polarization Effects on Observations With Low-Frequency Space Arrays," *The Astronomical Journal*, vol. 111, Jun. 1996, p. 2465.

[8] Duric, N., "Low-frequency radio astronomy and the origin of cosmic rays," American Geophysical Union, 2000, pp. 277–285.

[9] Kassim, N. E., and Yusef-Zadeh, F., "Long wavelength observations of supernova remnants," American Geophysical Union, 2000, pp. 287–296.

[10] Jester, S., and Falcke, H., "Science with a lunar low-frequency array: From the dark ages of the Universe to nearby exoplanets," *New Astronomy Reviews*, vol. 53, May 2009, pp. 1–26.

[11] Alexander, J. K., and Novaco, J. C., "Survey of the galactic background radiation at 3.93 and 6.55 MHz," *The Astronomical Journal*, vol. 79, Jul. 1974, p. 777.

[12] Alexander, J. K., Kaiser, M. L., Novaco, J. C., Grena, F. R., and Weber, R. R., "Scientific instrumentation of the Radio-Astronomy-Explorer-2 satellite," *Astronomy and Astrophysics*, vol. 40, 1975, pp. 365–371.

[13] Jones, D., Allen, R., Basart, J., Bastian, T., Dennison, B., Dwarakanath, K., Ericksong, W., Finley, D., Kaiser, M., Kassim, N., Kuiperl, T., Macdowall, R., Mahoney, M., Perley, R., Preston, R., Reiner, M., Rodriguez, P. O., Stone, R., Unwin, S., Weiler, K. O., Woan, G., and Wool, R., "The Astronomical Low Frequency Array : Explorer Mission for Radio Astronomy A Proposed Explorer Mission for Radio Astronomy," *Radio Astronomy at Long Wavelengths*, R.G. Stone, K.W. Weiler, M.L. Goldstein, and J.-L. Bougeret, eds., American Geophysical Union, 2000, pp. 339–349.

[14] MacDowall, R. J., Bale, S. D., Demaio, L., Gopalswamy, N., Jones, D. L., Kaiser, M. L., Kasper, J. C., Reiner, M. J., and Weiler, K. W., "Solar Imaging Radio Array (SIRA): A multi-spacecraft mission," *Enabling Sensor and Platform Technologies for Spaceborne Remote Sensing*, G.J. Komar, J. Wang, and T. Kimura, eds., 2005, pp. 284–292.

[15] Oberoi, D., and Pinçon, J.-L., "A new design for a very low frequency space borne radio interferometer," *American Geophysical Union Fall Meeting*, 2003, p. 17.

[16] Bentum, M., and Boonstra, A. J., "OLFAR - Orbiting Low Frequency Antenna for Radio Astronomy," *20th Annual Workshop on Circuits, Systems and Signal Processing, ProRISC*, 2009, pp. 1–6.

[17] Knapp, M., Babuscia, A., Jensen-clem, R., and Martel, F., "SOLARA / SARA : Solar Observing Low-frequency Array for Radio Astronomy / Separated Antennas Reconfigurable Array," *Innovative Ideas for Micro/Nano-Satellite Missions*, R. Sandau, S. Nakasuka, R. Kawashima, and J. Sellers, eds., International Academy of Astronautics (IAA), 2013, pp. 2–15.

[18] Wong, K. T., and Zoltowski, M. D., "Closed-form direction finding and polarization estimation with arbitrarily spaced electromagnetic vector-sensors at unknown locations," *IEEE Transactions on Antennas and Propagation*, vol. 48, 2000, pp. 671–681.

[19] Zatman, M., "How narrow is narrowband?," *IEEE Proceedings - Radar, Sonar and Navigation*, 1998, pp. 85–91.

[20] Meloling, J. H., Rockway, J. W., Daly, M. P., Monges, A. R., Allen, J. C., Nielsen, W. R., McGinnis, P. M., Thompson, R. B., and Mozaffar, N. A., *An Advanced HF Direction Finding Vector-Sensing Antenna System*, 2015.

[21] King, R., "The rectangular loop antenna as a dipole," *IRE Transactions on Antennas and Propagation*, vol. 7, Jan. 1959, pp. 53–61.

[22] Robey, F. C., Knapp, M., Fenn, A., Silver, M., Johnson, K., Lind, F. D., Volz, R., Seager, S., and Neylon-Azad, F., "High Frequency (HF) Radio Astronomy from a Small Satellite," *Small Satellite Conference*, 2016.

[23] Nordholt, E., and Van Willigen, D., "A new approach to active antenna design," *IEEE Transactions on Antennas and Propagation*, vol. 28, Nov. 1980, pp. 904–910.

[24] Grubb, R. N., Livingston, R., and Bullett, T. W., "A new general purpose high performance HF Radar (Adapted from the 2008 URSI General Assembly Commission G Submission and Presentation)."

[25] Gorski, K. M., Hivon, E., Banday, A. J., Wandelt, B. D., Hansen, F. K., Reinecke, M., and Bartelmann, M., "HEALPix: A Framework for High-Resolution Discretization and Fast Analysis of Data Distributed on the Sphere," *The Astrophysical Journal*, vol. 622, Apr. 2005, pp. 759–771.

[26] Knapp, M., Robey, F. C., Volz, R., Lind, F. D., Fenn, A., Morris, A., Silver, M., Klein, S., and Seager, S., "Vector Antenna and Maximum Likelihood Imaging for Radio Astronomy," *IEEE Aerospace*, 2016.

[27] Lind, F. D., Lonsdale, C. J., Faulkner, A. J., Alexander, P., and Mattmann, C., "Radio array of portable interferometric detectors (RAPID)," *2013 IEEE International Symposium on Phased Array Systems and Technology*, IEEE, 2013, pp. 676–683.

[28] Volz, R., Knapp, M., Lind, F., and Robey, F., "Covariance Estimation in Terms of Stokes Parameters with Application to Vector Sensor Imaging," *50th Asilomar Conference on Signals, Systems and Computers*, Pacific Grove, CA: 2016.

[29] Högbom, J. A., "Aperture Synthesis with a Non-Regular Distribution of Interferometer Baselines," *Astronomy and Astrophysics Supplement*, vol. 15, 1974.

[30] Carozzi, T. D., "Imaging on a sphere with interferometers: the spherical wave harmonic transform," *Monthly Notices of the Royal Astronomical Society: Letters*, vol. 451, May 2015, pp. L6–L10.

[31] Shaw, J. R., Sigurdson, K., Pen, U.-L., Stebbins, A., and Sitwell, M., "All-Sky Interferometry With Spherical Harmonic Transit Telescopes," *The Astrophysical Journal*, vol. 781, 2014, p. 57.

[32] Haslam, C. G. T., Salter, C. J., Stoffel, H., and Wilson, W. E., "A 408 MHz all-sky continuum survey. II - The atlas of contour maps," *Astronomy and Astrophysics Supplement Series, vol. 47, Jan. 1982, p. 1, 2, 4-51, 53-142.*, vol. 47, 1982, p. 1.

[33] Remazeilles, M., Dickinson, C., Banday, A. J., Bigot-Sazy, M.-A., and Ghosh, T., "An improved source-subtracted and destriped 408 MHz all-sky map," *Monthly Notices of the Royal Astronomical Society, Volume 451, Issue 4, p.4311-4327*, vol. 451, Oct. 2014, pp. 4311–4327.

[34] NIST, "Radio Station WWV" Available: http://www.nist.gov/pml/div688/grp40/wwv.cfm.